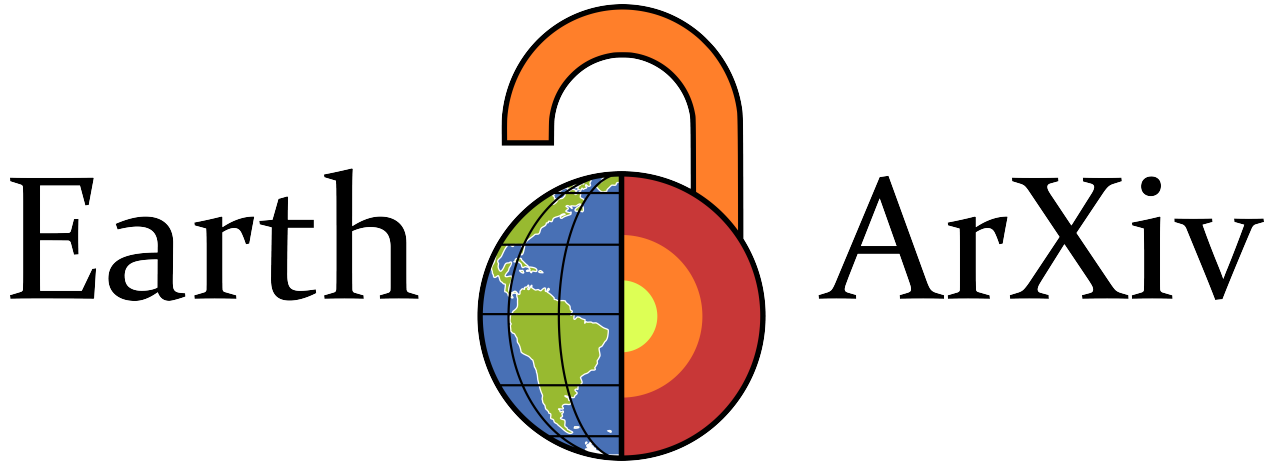

Non-peer reviewed Report submitted to Seismica: Correlation of DAS Strain Data and Oceanographic Variables in the North-East Atlantic

David Schlaphorst * [1,2], **Luís Matias** [1], **Afonso Loureiro** [1,3], **Athanasia Papapostolou** [4], **Carlos Corela** [1], **Susana Gonçalves** [1], **Rui Caldeira** [3]

[1]IDL - Instituto Dom Luiz, Faculdade de Ciências, Universidade de Lisboa, Lisboa, Portugal, [2]Instituto Superior de Engenharia de Lisboa, Lisboa, Portugal, [3]Agência Regional para o Desenvolvimento da Investigação, Tecnologia e Inovação, Funchal, Portugal, [4]Hellenic Centre for Marine Research, Anavyssos, Attica, Greece

Author contributions: *Conceptualization*: DS, LM, AP. *Methodology*: DS. *Software*: DS. *Formal Analysis*: DS. *Writing - Original draft*: DS. *Writing - Review & Editing*: DS, LM, AL, AP, CC, SG, RC. *Funding acquisition*: LM, RC.

Abstract Distributed Acoustic Sensing (DAS) recordings close to the coast are influenced by pressure signals from land- and seaward ocean surface gravity waves. The amplitude and period of the signal can serve as proxies for the sea state. Measurements along the cable at greater water depths show secondary microseisms related to the sea state away from the shore. The significant wave height (SWH) and ocean currents along the cable can be evaluated continuously during the experiment, resembling a dense sampling array of closely spaced moored buoys. However, in order to provide serviceable results, the measurements have to be calibrated against an existing buoy or wave numerical model data. In October 2023, the GeoLab dark fibre off Madeira Island in the Atlantic was fitted with a DAS interrogator under a project by ARDITI and the Oceanic Observatory of Madeira. As a pilot site, the experiment is linked to the SUBMERSE project that is trying to establish continuous DAS monitoring along fibre-optic cables at multiple locations around Europe. We use a one-week recording in late 2023, as well as a 5-day interval in 2024, to show changes in the DAS data close to the shore where the water depth is small. Spectrograms of individual channels and *f-k* spectra of different time intervals show effects of varying sea states, such as currents on the dispersion curves between land- and seaward waves. To calibrate the measurements, the data are compared against measurements from a moored buoy located close to the coast and the DAS cable. We use data from the Atlantic-Iberian Biscay Irish-Ocean Wave Analysis and Forecast, which shows good correlation with the buoy data, but lacks the small-scale variations that can be observed with buoy point measurements.

*Corresponding author: dschlaphorst@fc.ul.pt

1 Introduction

The observation of hydrodynamic processes close to the shore is an important tool to assess variations in the flow of ocean water governed by forces such as tides and wind. Since these processes act on different spatiotemporal scales, both , and therefore have varying impacts, accurate measurements would ideally require a wide range of measurements that can capture relatively fast-changing small-scale observations, as well as longer-term changes on broader scales. Furthermore, to be of use for hazard assessment and early warning systems, real-time in-situ monitoring would be needed. Moored oceanographic buoys are able to provide continuous measurements of ocean state parameters, such as significant wave height (SWH), wave period, and ocean currents along the cable. These measurements provide vital input to larger-scale ocean circulation models. However, the instruments can only provide spatially limited observations, and dense coverage along larger sections of coast lines is often not feasible, as it often provides logistical challenges and is normally costly. On the other hand, satellite data can cover large-scale monitoring, for example ocean surface waves, but might not be able to capture more complex patterns in shallower regions close to the shore due to temporal and spatial resolution limits.

To satisfy the need for nearshore high spatial and temporal resolution monitoring of oceanographic parameters in real time, the addition of observations using submarine telecommunication fibre-optic cables can be of great help (e.g., Howe et al., 2019). Changes in strain, pressure, and temperature affect the propagation of light along the fibre, as well as the way energy is backscattered (Hocker, 1979; Hamza et al., 2004; Seabrook et al., 2022; Peláez Quiñones et al., 2023; Becerril et al., 2024). Light pulses travelling along the fibre are predominantly backscattered by elastic Rayleigh scattering, which is used by Distributed Acoustic Sensing (DAS) to characterise the acoustic field in terms of amplitude, wavelength, and phase over a wide dynamic range (Lindsey et al., 2020). Due to these characteristics, DAS is able to provide broadband strain measurements on very small spatial and temporal scales that would be difficult to achieve with traditional instruments.

In the last decade, technological advancements have led to different uses of fibre-optic sensing to observe influences due to earthquakes, but also due to oceanographic processes, such as tides and waves (e.g. Lindsey et al., 2019; Marra et al., 2022; Zhan et al., 2021). In many settings, the implementation could be cost- and time-effective by making use of already existing fibre-optic telecommunication cables and, in the last years, the implementation in oceanographic settings has been successful in monitoring distant storms (Landrø et al., 2022; Rørstadbotnen and Landrø, 2025), and ocean surface gravity waves (OSWG) (e.g., Sladen et al., 2019; Williams et al., 2019, 2022).

Sections of the cable close to the coast are particularly well-suited to monitor the sea state, since the deformation signal in shallow waters is dominated by pressure oscillations from ocean surface gravity waves, which decay exponentially with depth (Williams et al., 2019). While ocean currents have been monitored with DAS data, using oscillations at suspended marine cable sections (Flores et al., 2023), current values have also successfully been retrieved by observing differences in the dispersion curves of land- and seaward waves (Williams et al., 2019). Using a similar approach and monitoring the variation in dispersion curves over time, Song et al. (2024) were able to match current observations to tidal effects. In addition, the effect of wave incidence angles relative to the cable on dispersion curves can be observed (Sladen et al., 2019).

Ideally, a combination of established point measurements from buoys and emerging broader-scale measure-

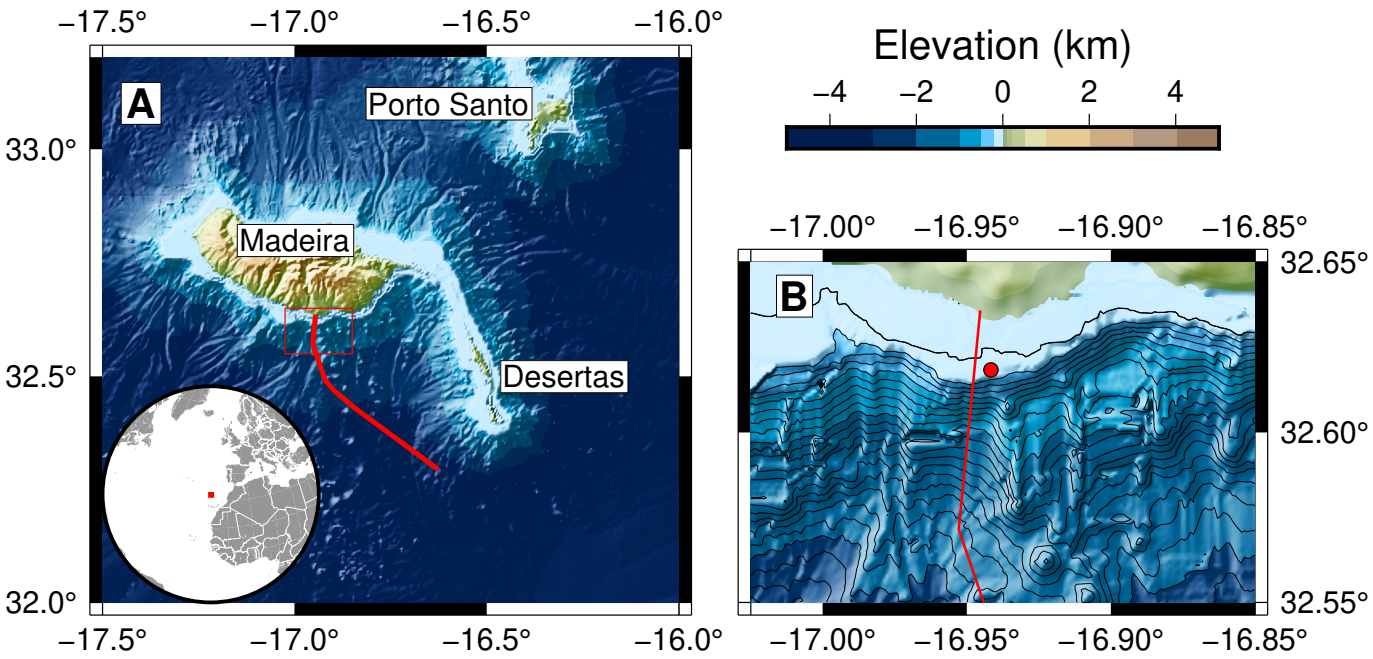

Figure 1 Map of the Madeira archipelago. (A) Map showing the entire archipelago and approximate cable position (red line). (B) Details of the first few marine kilometres of the approximate cable position (red line; 16.941 66°W, 32.618 33°N) and buoy that was active during the observation time window in 2023 (red circle) south of Madeira. Bathymetry contours are shown for every 100 m of seafloor depth with the depth of 100 m being marked by a thicker black line. Topography and bathymetry taken from GEBCO Compilation Group (2023).

ments using DAS could provide high-resolution in situ observations of complex wave fields needed for accurate real-time assessment of the near shore sea state. Besides that, however, once results obtained with DAS are calibrated against buoy measurements, or numerical models and reanalysis satellite-based products, it is possible to estimate the sea state solely based on measurements on the continuous fibre (e.g., Marra et al., 2018, 2022; Guo et al., 2023; Glover et al., 2024) .

In this study, we observe the ocean state south of Madeira Island in the Atlantic (Fig. 1) using a week of data from a DAS fibre-optic cable as part of the SUBMERSE project ("SUBMarine cablEs for ReSearch and Exploration"). One aim of the project is to correlate the amplitude and period of the DAS signal with the sea state to serve as a proxy. For that, the data must be calibrated against measurements from adjacent buoys and wave model data. We use a buoy, which has a distance to the cable of less than 1 km, while the Atlantic-Iberian Biscay Irish - Ocean Physics Reanalysis (IBI) has a grid resolution of $0.0278° \times 0.0278°$ (Toledano et al., 2022).

2 Data and Method

2.1 The DAS fibre

The data used in this study was taken from a GeoLab fibre (Loureiro et al., 2025) off the southern coast of Madeira Island (Fig. 1). The data is a continuously recorded stream with a sampling frequency of 500 Hz between October 27th and November 3rd 2023. The interrogator recorded the phase differences with a gauge length of 10.2 m, which corresponds to the average strain measurement over 10 instrument channels, with a spacing of 5.1 m, leading to an overlap of around 50 %. The entire cable holds a total of 11 380 channels, stretching over a distance of about 57 km. Further details can be found in Loureiro et al. (2025).

The pressure of ocean surface gravity waves can be observed on the first marine kilometres of the fibre where the

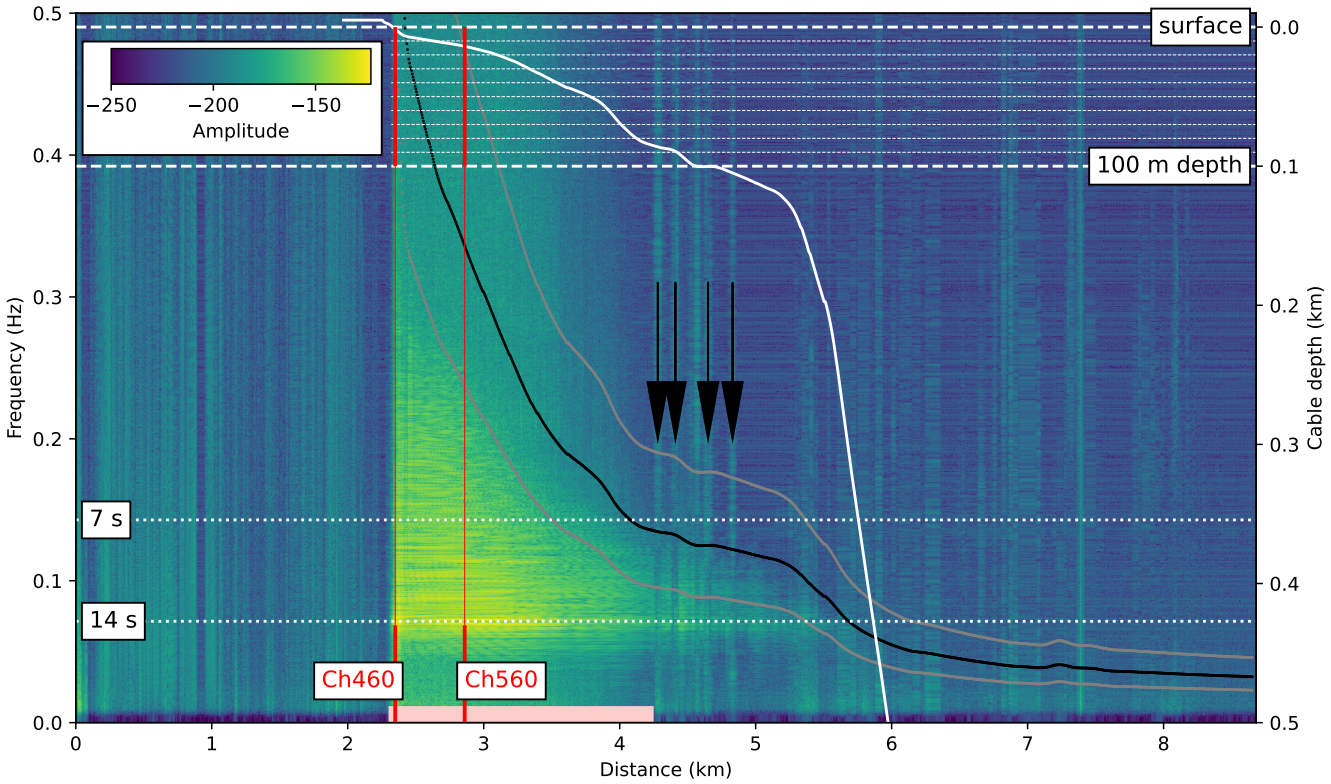

Figure 2 Median power spectral density of every channel in the first 1700 channels for a DAS recording over a 30-minute interval (start time: 27/10/2023 15:29:58 GMT), downsampled to 1 Hz and highpass filtered with a corner frequency of 0.01 Hz. The depth of the cable is shown in white, between the surface and 100 m depth white horizontal dashed lines are shown every 10 metre. The calculated f_c are shown with a black line for a wavelength to water depth ratio of 1 (Williams et al., 2022) and with grey lines for limits of 0.5 and 2 (Crawford et al., 1991). Black arrows point to sections with low SNR. The section of the cable useful for this study is indicated with a light red bar between 2.3 km and 4.3 km. The channels predominantly used in this study (460 to 560) are indicated by vertical red lines. Figure adapted from Loureiro et al. (2025).

seafloor is shallow, which is consistent with previous studies in different regions (Sladen et al., 2019; Williams et al., 2019, 2022). Around Madeira, the steep bathymetry only provides a stretch of around 2 km, where the signal can be identified (Fig. 2). Between 4.3 km to 5 km, several channels show low signal-to-noise ratio (SNR), likely due to bad coupling of the cable to the ground Therefore, we do not use that part of the cable. The data quality at all channels along the previous 2 km is good, while a dataset decimated to 1 Hz with a spatial sampling of 10 m provides dense coverage. There is a general trade-off between working with high signal-to-noise ratio (SNL) data by stacking adjacent stations and providing results with high spatial resolution by reducing the number of combined channels. Due to the steep topography and bathymetric complexity close to the coast, we only use 100 marine channels, excluding the very first marine channels to ensure constant water coverage at low tide as well (460 to 560; covering ∼510 m distance).

In the first 10 km the cable traverses three distinctly different domains: on land (channels 0 to 450), in water on a shallow shelf close to the coast (channels 450 to 800), and in deeper water (Fig. 2). The domain in shallow water shows a prominent peak at 14 s, which vanishes at a distance where the water depth is greater than ∼100 m,in agreement with Williams et al. (2022). In contrast to that study, we do not observe a second prominent peak at 7 s. The Madeira cable offers about 2 km in the shallow marine part with a visible peak at 14 s and good SNR. The frequency at which the signal of OSWGs falls below the instrumental noise floor, also known as f_c is described by:

$$f_c = \sqrt{\frac{g}{2\pi h n}} \quad , \tag{1}$$

where n defines the relation between wavelength and water depth and is in the range of 0.5 to 2 (Crawford et al., 1991; Williams et al., 2022).

When applying a Fourier Transform to time sections of parts of the data, it is possible to separate apparent movement along the cable in either direction, based on the wavenumber. In our case, based on the geometry of the cable close to the shore, we define them as landward and seaward. To ensure both high temporal resolution, as well as good SNR, we take the Fourtier transform in half-hour intervals. The half-hour *f-k* spectrograms of the cable section on the narrow shelf show a strong dominance of landward waves (Fig. 3), which is a stable pattern over all observation days.

2.2 Theoretical dispersion of OSWG

In the shallow marine section the phase velocity of the OSWG can be used to calculate a relationship between wave number and frequency:

$$\omega^2 = gk \tanh(kh) \quad . \tag{2}$$

The equation describes a theoretical dispersion curve (TDC) with ω as the angular frequency, g as the gravitational acceleration, k as the angular wave number, and h as the water depth. For the 100 marine channels close to the coast used in this study, we have a variation in h from 5.0 mto 14.5 m. A current will act directionally, therefore distorting both the land- and seaward side branches of the TDC at the same time into either the land- or seaward direction (Williams et al., 2019). This can be expressed by including an additional parameter, U, describing the apparent velocity of the current along the cable:

$$(\omega - Uk)^2 = gk \tanh(kh) \quad . \tag{3}$$

So far, a wave direction parallel to the cable is assumed, which in case of the GeoLab fibre and most marine fibre-optic cable deployments, is almost perpendicular to the coast line. However, a different incidence angle of the wave train on the cable can affect the TDC (Sladen et al., 2019). For different incidence angles (θ), the wave number k can be replaced by k_{inc}, so that

$$(\omega - Uk)^2 = gk \tanh(k_{inc}h) \quad , \tag{4}$$

with

$$k_{inc} = \frac{k}{\cos(\theta)} \quad , \tag{5}$$

As can be seen from Eqs. (4) and (5), ocean currents and incidence angles have different effects on the TDC. Whereas currents shift both branches (land- and seaward) towards one wavenumber direction (e.g., Williams et al.,

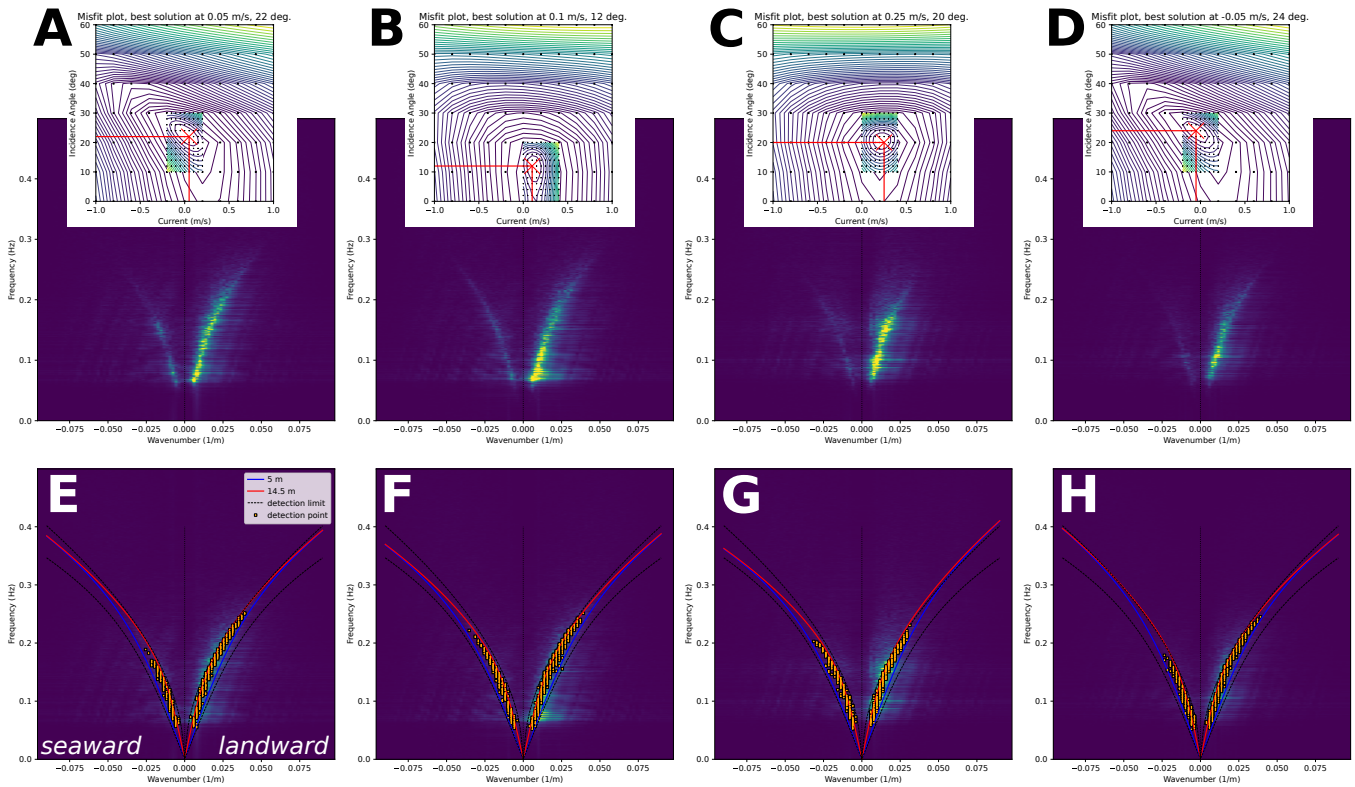

Figure 3 TDC calculations for different half-hour data, showing *f-k* spectra and grid search misfit calculations, at channels 460 to 560, with data downsampled to 1 Hz, with start times of A,E) 27/10/2023 10:29:59 GMT, B,F) 27/10/2023 17:29:59 GMT, C,G) 29/10/2023 15:59:59 GMT, D,H) 1/11/2023 14:59:59 GMT. The landward side is represented by positive wavenumbers and the seaward side is represented by negative wavenumbers. The top panels (A-D) show the data in *f-k* space, together with the grid search results as insets, indicating the best solution by red lines, and the bottom panels (E-H) show all the detection points on top of the data, together with the detection limits and the calculated TDC for the shallow and deep solution of the cable section.

2019), an increased incidence angle leads to both branches being compressed towards the $k = 0$ axis. Therefore, we can perform a grid search to find the minimum misfit between the model and the data.

2.3 Misfit calculation

It is evident from the hyperbolic tangent that water depth variations at shallower levels have a much stronger influence on the shape of the TDC than variations of the same magnitude in deeper water. Especially at depths shallower than 100 m the change is significant. Therefore, we introduce two TDCs, representing the channel with the minimum water depth (generally the channel closest to the coast) and the channel with the maximum water depth (generally the channel furthest away from the coast). We then calculate the misfit between both TDCs and the detection points as a squared distance in *f-k* space.

In addition, individual misfit values are weighted by the signal amplitude relative to the strongest amplitude on the respective wavenumber side. The edge that needs to be fitted by the curve is located directly adjacent to the strongest values on the outside (we define "outside" as being away from the $k = 0$ axis and "inside" as being towards the $k = 0$ axis). To account for this, we introduce an additional adjustment factor that is applied to the misfit, in case the TDC is inside the detection points. Our tests show that 2 is sufficient as an adjustment factor. A larger factor will always push the TDC to a state of $\theta = 0$ and, although wave fronts generally orient themselves orthogonal to the steepest gradient and thus more or less parallel to the coastline (Herbers et al., 1999; Szczyrba et al., 2023), an

incidence angle of $0°$ to the cable is unlikely.

To save computation time, the grid search is performed in two steps, first with a coarse and second with a finer grid. The coarse grid ranges from ocean currents of $-1.0\,\mathrm{m\,s^{-2}}$ to $1.0\,\mathrm{m\,s^{-2}}$ in increments of $0.2\,\mathrm{m\,s^{-2}}$ and incidence angles of $0°$ to $60°$ in increments of $10°$. The fine grid is afterwards placed around the solution with the lowest misfit (v_{low}, θ_{low}), at $v_{low} - 0.2\,\mathrm{m\,s^{-2}}$ to $v_{low} + 0.2\,\mathrm{m\,s^{-2}}$ in increments of $0.05\,\mathrm{m\,s^{-2}}$ and from $\theta_{low} - 10°$ to $\theta_{low} + 10°$ in increments of $1°$. Due to the constant variation of the TDC in both dimensions on the error surface (current, incidence angle) and the detection point distribution close to line features along the shape of the dispersion curves, we do not expect secondary local minima, and a priori tests using a fine grid search on the entire error surface, support this condition.

2.4 Phase velocity detection

There are different ways to detect the phase velocity on the land- and seaward side at each frequency.

One way is to treat the individual frequencies as a seismic trace, on which an STA/LTA picker (Allen, 1978) can be used, calculating the lower edge by applying the picker in positive and negative x-axis directions (Song et al., 2024). This algorithm is able to capture the majority of the outer edges of the areas with higher amplitudes between 0.05 Hz to 0.25 Hz (Fig. S1A), but also includes random detections from outside that range. Song et al. (2024) discard those points based on significant deviations from their TDC during the fitting, but we find that an improvement could also be achieved by introducing an amplitude based mask (Fig. S1B). For every frequency, we compare the maximum amplitude on the land- and on the seaward side with the overall maximum amplitude on the respective side and discard all detection points where the ratio falls beneath a threshold value. This threshold might need to be adjusted for different settings, including cable depth close to the coast, due to the dominance of the strongest amplitudes.

Based on the general shape of phase velocity curves, we also test picking algorithms that detect the maximum amplitude per frequency on either side (Fig. S1C) and the point of maximum amplitude change outside the maximum point (Fig. S1D). All detection algorithms have similar computation times of around 2 to 5 seconds, which makes computation in real time possible. The latter two algorithms yield very similar results, which in general have fewer outliers from the main shape of theoretical dispersion curves. In addition, they are simpler to combine with further modifications.

One such modification is the introduction of a search limit based on theoretical dispersion curves. Especially on the landward side (positive wavenumbers) at 0.15 Hz to 0.25 Hz a diffuse cloud of higher amplitude values can be observed inside the maximum amplitude values (Fig. 3) and are also picked up by all three algorithms (Fig. S1B-D). This can be caused by different wave train incidence angles, as well as overall bathymetric complexities at shallow seafloor depths. By limiting the search to different sections of the *f-k* spectrum, it is possible to individually estimate the dispersion curves for two superimposed settings. In this work, we focus on the main branch by masking the diffuse cloud.

2.5 Correlation of SWH & Mean Wave Period to the data

Using ocean-bottom seismometer (OBS) data over a time of almost one year, (Corela, 2014) showed that variations of significant wave height estimated by a model are comparable to the behaviour of power spectra peaks at periods of 4 s to 8 s. The mean wave period peaks correlate with the peaks of the second microseism in the power spectrum over

270 days. Although the values do not match perfectly, sometimes over a number of days, the overall comparability is evident when comparing on a broader time frame.

We can use the same methods for our data. However, it should be noted that our observation time windows are significantly shorter, and time intervals of similar length have been found by Corela (2014) without correlations. Therefore, our results should be interpreted with caution.

2.6 Maximum amplitude measurements in *f-k* space

In addition to the observation methods discussed so far, a more straightforward measurement can be taken on the half-hour *f-k* spectra of the first 100 marine channels of the DAS fibre. In contrast to fitting the TDC, as demonstrated in the previous parts, it is possible to extract information of the maximum amplitude (regardless of frequency or wavenumber of that particular value) on the land- and seaward side. These values can then be compared to oceanographic parameters as well to establish correlations.

3 Results

3.1 Characteristics and temporal variations of half-hour TDCs

In general, the landward branch of the TDC in *f-k* space is always stronger than the seaward branch, regardless of any of the oceanographic parameters (Fig. 3, and the often observed "diffuse cloud" can only be spotted on the landward side. Throughout the two observation periods we can observe significant changes in the shape and amplitudes of the two branches. We notice periodic changes in the shape of the time scale of tidal patterns, which can be investigated further using TDC fitting and maximum amplitude observation. Significant changes between different days in the TDC amplitudes and complexities especially on the landward side can be observed, hinting towards influences of the sea state on the data, which can also be investigated in more detail.

3.2 Mean Ocean Current from TDC matching

The ocean current estimated by fitting the TDC to the half-hour data of the first 100 marine channels shows variations between $-0.1\,\mathrm{m\,s^{-1}}$ and $0.3\,\mathrm{m\,s^{-1}}$ in both time intervals (Figs. 4A and 5A). Here, the values are apparent current velocities along the cable in the landward direction, with negative values representing the apparent seaward direction. Apart from a brief period on 1/7/2024, they do not correlate with tidal patterns. Furthermore, they do not correlate with SWH, dominant wave incidence angle, or mean wave period.

3.3 Wave Train Incidence Angle from TDC matching

During both observation periods, the wave train incidence angle was measured between 10° and 30°, with 0° being parallel to the cable (Figs. 4B and 5B). The values correlate very well with the tide information in the area, in both periods showing a correlation with the height of the tide (h_t) of $\theta_{inc} \sim \frac{20}{3} h_t + 1$. The biggest deviations from those correlations can be observed on 1/7/2024, on the day when the ocean current correlates best with the tide height values.

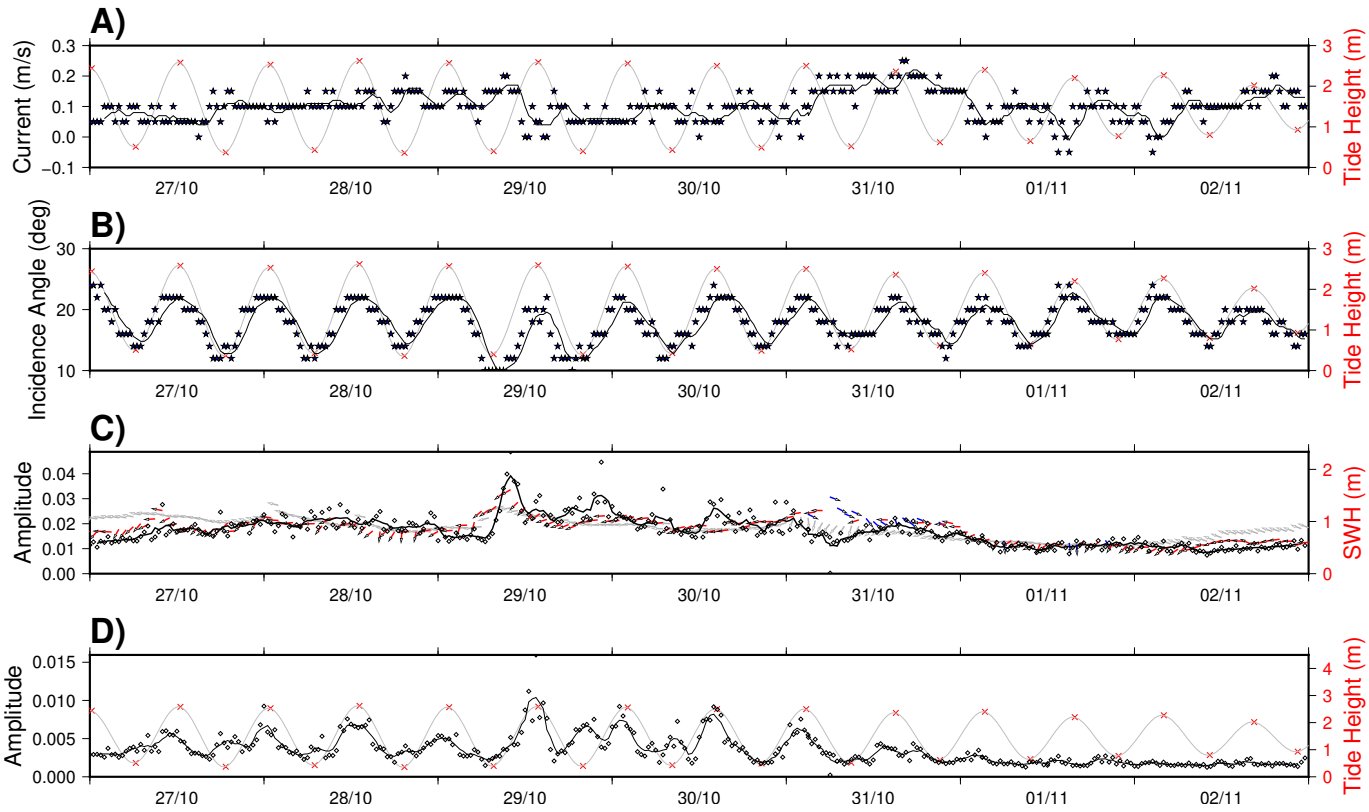

Figure 4 Results of DAS observations against oceanographic parameters for the 7-day period in 2023. (A) Oceanic current from DAS dispersion curve fitting against tide values. Blue stars show individual 30-minute measurements, the black line show a rolling 5 measurement average. Red crosses show tidal values for Funchal, which is close to the landing site of the cable, grey lines show sine interpolations between those values. (B) Dominant wave incidence angle from DAS dispersion curve fitting against tide values. (C) Maximum amplitude values of landward waves against SWH (arrow amplitude) and mean wave direction (arrow direction). The measurements are taken from the closely located buoy (red for western and blue for eastern directions) and from the IBI data (grey). (D) Maximum amplitude values of seaward waves against tide values.

3.4 Maximum amplitude on landward side

Unlike Corela (2014), we cannot find a correlation between SWH as measured by a buoy located close to the cable location near the coast of Madeira (Fig. 1) and the power spectra peaks at specific periods, likely because the DAS data used in our study only cover two time windows of 7 and 5 days, which is too short to establish similar fits.

However, we find that the maximum amplitude of the landward side of the half-hour *f*-*k* spectra correlates very well with the SWH measurements of the nearby buoy (Figs. 4C and 5C). The mean calibration factor, comparing the results to the data, over the entire 2023 time interval is 47.9, although the values differ slightly by day (between 43.3 on 30/10/2023 to 52.6 on 27/10/2023 and 2/11/2023; Table 1). Differences on 30/10/2023 can be found but coincide with a change in mean wave direction. As can be seen in the 2023 data, the IBI, while showing a general trend that has similarities to the amplitude, does not carry the small-scale details that can be observed and correlated, resulting in a larger variation in the calibration factor (39.6 on 30/10/2023 to 63.4 on 2/11/2023). Unfortunately, the buoy was not operational during the second observation period in 2024. The mean calibration factor is 46.5.

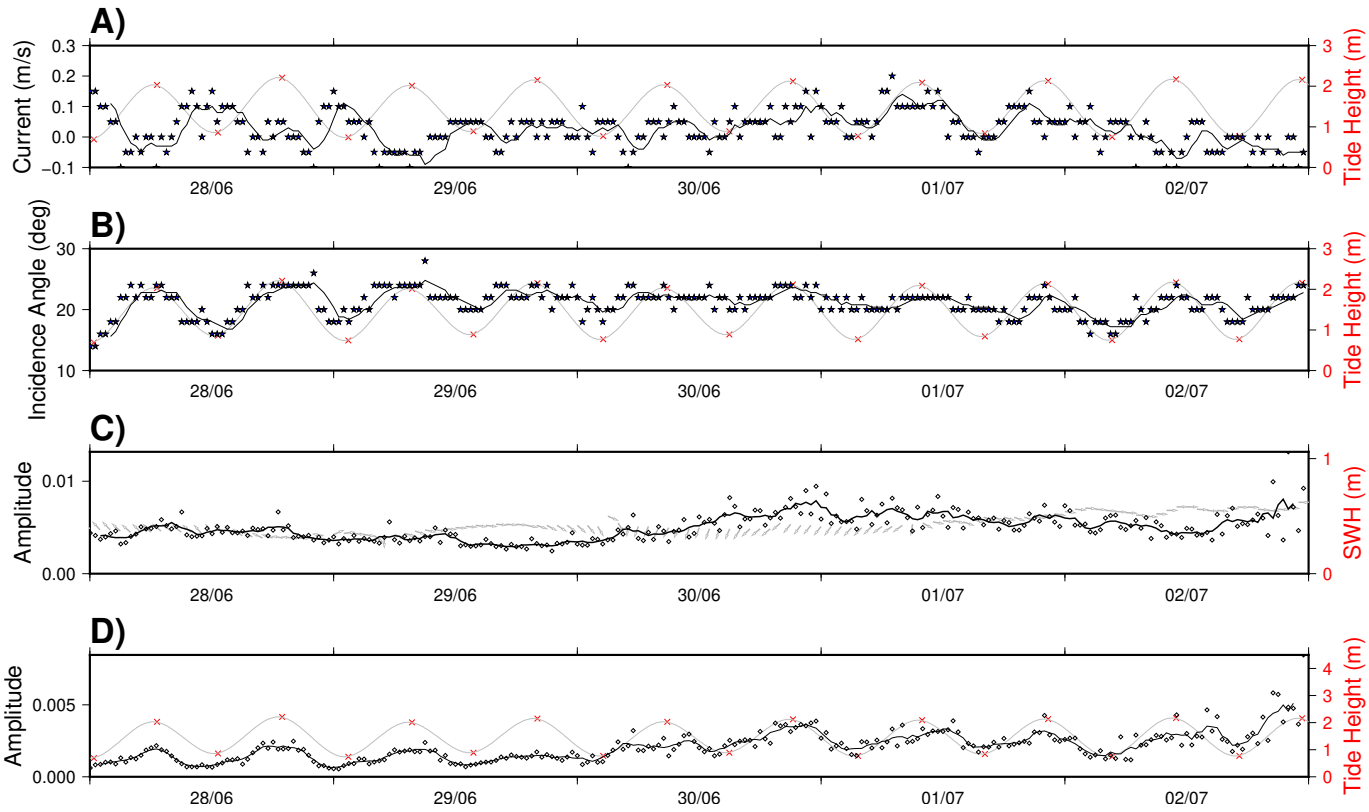

Figure 5 Results of DAS observations against oceanographic parameters for the 5-day period in 2024. See Fig. 4 for explanations. For panel C note, that the buoy was not operational during this time interval.

3.5 Maximum amplitude on seaward side

On the seaward side, the maximum amplitude is between 1/2 and 1/6 of the amplitude on the landward side (Figs. 4D and 5D). In both observation windows, the amplitudes generally correlate with the tide information. However, the general calibration factor between the values for 2023 and 2024 is not the same, and even changes throughout the two time periods. During the days with the highest landward maximum amplitudes (29/10/2023 and 30/6/2024), as well as highest SWH in case of the 2023 observation, the patterns significantly deviate. Furthermore, calm periods with very low amplitudes can be observed (1/11/2023 to 2/11/2023), where no correlation is present. In contrast, on days of prolonged periods of agitated sea state (1/7/2024 to 2/7/2024), the correlation is shifted to a different calibration factor.

3.6 Mean Wave Period

Observing the power spectra of channels close to the coast over both time intervals (Fig. 6), the effects of tides and storms can be probed over various days. The effect of tides is visible as amplitude frequency shifts with a duration of around 6 h in the range of 16 Hz to 22 Hz. In addition, high-amplitude anomalies that change in frequency from around 18 Hz to 10 Hz over a span of several days can be observed and attributed to storms. Although the peaks in the mean wave in 2023 do not correlate with peaks in the power spectrum similar to Corela (2014), likely due to the short observation time window, there is a noticeable decrease in the mean wave period observed by the buoy on 29/10/2023. Its relation to a storm is not clear and could be investigated in more detail once additional data with additional storms are available. Also, the shape of the bay might influence the flow current and wave patterns significantly.

Table 1 Calibration factors between the maximum amplitude measurements on the landward side with the SWH measurements from the buoy, with the SWH values of the IBI re-analysis, and the seaward side with tide values.

Date	Land–SWH (buoy)	Land–SWH (IBI)	Sea–Tide
27/10/2023	52.9	60.0	353.7
28/10/2023	44.0	45.8	340.5
29/10/2023	44.1	41.1	259.2
30/10/2023	43.3	39.6	312.1
31/10/2023	59.5	48.9	437.5
01/11/2023	51.8	48.0	740.4
02/11/2023	52.6	63.4	882.5
Average 2023	47.9	46.5	354.1
28/06/2024	—	75.4	1064.2
29/06/2024	—	103.3	1129.6
30/06/2024	—	73.3	605.0
01/07/2024	—	72.2	555.8
02/07/2024	—	88.8	473.2
Average 2024	—	80.3	618.8

4 Discussion

4.1 Theoretical Dispersion Curve matching

The grid-search fitting approach demonstrates the different influences of oceanographic parameters on the TDC shape, with variations in the oceanic current and the dominant wave train incidence angle not correlated with each other. The cyclic variations in incidence angles strongly correlate with tidal patterns during both observation periods. The values are between 10° to 30°, which indicates a subparallel alignment with the coast. These alignments are to be expected during the general low-energy conditions on those days, due to the decrease in water depth close to the shore (Herbers et al., 1999; Szczyrba et al., 2023). Variations in angle can be explained by the setting of the Praia Formosa bay, where the cable reaches the water and continues along the shallow shelf.

In contrast, the strength of the ocean current does not show an overall correlation with tides, even though influences could be seen in other regions (e.g., Song et al., 2024). However, it is likely that further influences, especially caused by the complex subsurface structure close to the coast, could be superimposed. Current wakes caused by the deflection of currents due to bathymetric complexity are also likely to play a role (Caldeira et al., 2005). Therefore, it is understandable that some correlation can be observed (1/7/2024), which could be caused by a more agitated sea state during the time of a passing storm, thus increasing the proportion of this influence. However, a similar pattern could not be observed during a similar situation in the first observation window (30/10/2023). A further, longer time period would be needed to increase our understanding.

Although ocean currents and wave train incidence angles are among the strongest influences on the shape of the TDC, there are other potential influences, such as complexities in bathymetry and resulting current patterns especially close to the coast. Those complexities are predominantly observed on the landward side, where the amount of energy is significantly higher.

4.2 Maximum amplitude variation observation

As a first-order observation, much stronger amplitudes are found on the landward side of the *f-k* spectrum. This can be explained by the majority (>90 %) of the incident wave energy being dissipated close to the shore by wave breaking

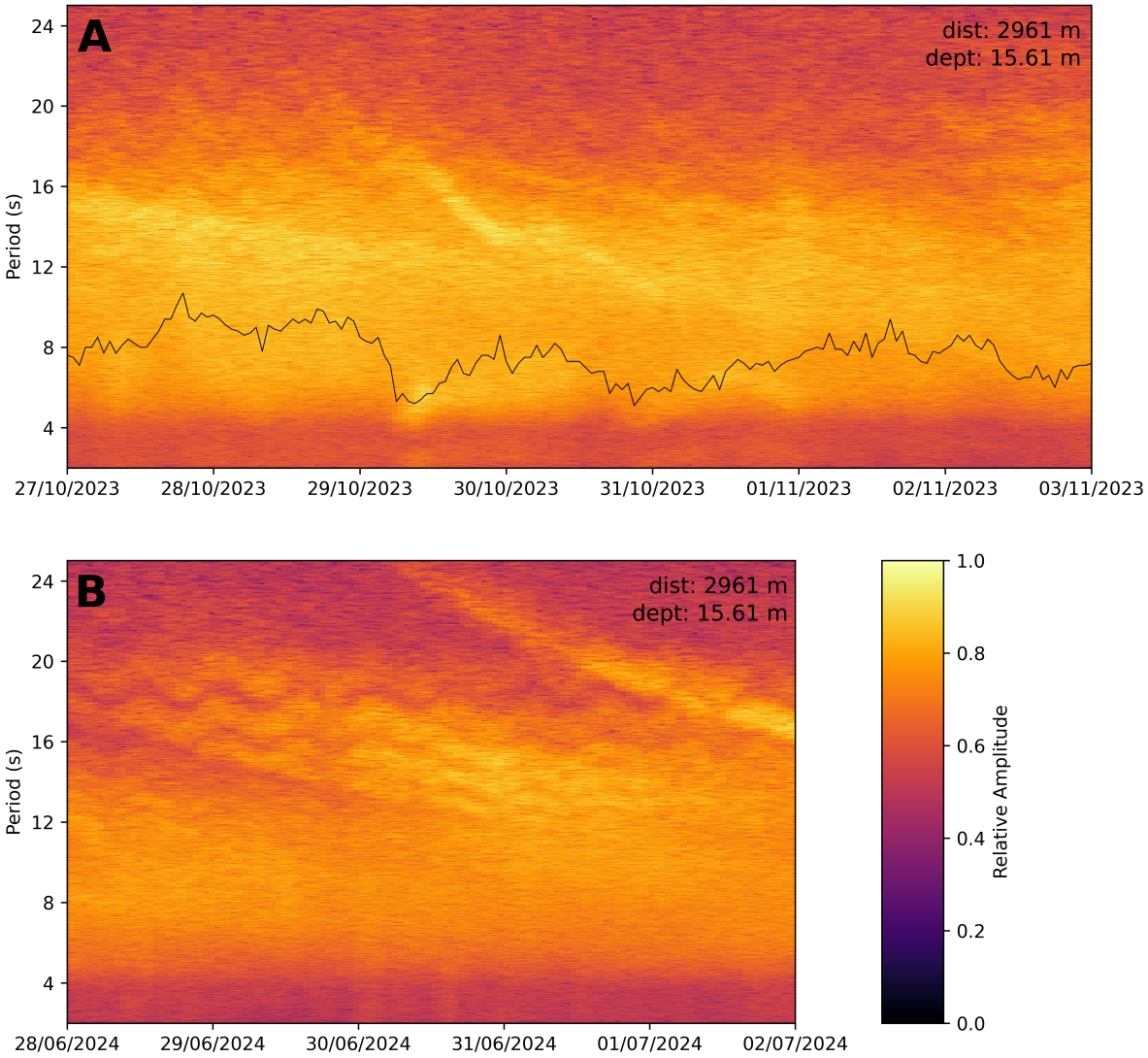

Figure 6 Power spectra over the seven-day period in 2023 (A) and the five-day period in 2024 (B) for channel 580 at 2961 m from the starting point (∼600 m from the coast) with a seafloor depth of 15.61 m, using 214 samples per Fourier transformation. The Fourier spectrum was calculated with a sample bin size that approximately matches one measurement every hour to be comparable to the hourly buoy data. The relative amplitudes are computed over both time intervals combined to make the figures comparable. The black line depicts the mean wave period as measured by the buoy in 2023.

(Elgar et al., 1994), resulting in weaker reflected waves.

We find a strong correlation between SWH measured by a buoy in close proximity and the maximum amplitude on the landward side of the TDC in *f-k* space. The correlation even matches changes over single points of measurement, representing half an hour, which can only be resolved by the buoy measurement and does not show up in regional reanalysis data or the 2.5-hour rolling average (Fig. 4C). The amplitudes are further influenced by the mean wave direction, resulting in worse correlations on a day where the direction is changing (31/10/2023).

A correlation between the maximum amplitude on the seaward branch of the TDC can also be observed in both

time intervals. However, in contrast to the dominant wave train incidence angle results, these values show stronger influences by other parameters, such as a general amplitude increase due to a more agitated sea state during days of passing storms (29/10/2023 to 30/10/2023 and 30/6/2024). Likewise, on calmer days the pattern can fall below the noise threshold (1/11/2023 to 2/11/2023).

5 Conclusions

In this study, we worked with two short time intervals of data on a dark fibre south of Madeira Island, Atlantic, and used around half a kilometre of marine channels close to the coast to find proxies for oceanographic variables. Due to the different influences of the ocean current and wave train incidence angle on the shape of the TDC, we are able to use a grid search approach to fit the model to the data.

We find strong correlations between tides and dominant wave train incidence angles, as well as SWH and maximum amplitude measurements in *f-k* space. No definite trends could be observed between the mean wave period taken from the buoy data and the DAS power spectrum, likely due to the short time interval.

All processes have short computation times that allow for an automated run in real time. Furthermore, the processes are easily adaptable to different settings, as well as to different data. This allows for their implementation at other sites. In addition, longer time intervals, also including different sea states, would be beneficial to calibrate and test the approach further.

Acknowledgements

The authors would like to thank Susana Custódio for many fruitful conversations and suggestions that helped to improve the article. ObsPy (Beyreuther et al., 2010) and Generic Mapping Tools (Wessel et al., 2019) were used in the processing of data and creation of figures. This work was funded by the Portuguese Fundação para a Ciência e a Tecnologia (FCT) I.P./MCTES UID/PRR/50019/2025, by MODAS project 2022.02359.PTDC, and by the EC SUBMERSE project GA 101095055. The authors also acknowledge support from the Geo-INQUIRE (GA 101058518) project. SUBMERSE is funded by the European Commission under grant agreement number 101095055 within the HORIZON-INFRA-2022-TECH-01 call. Geo-INQUIRE is funded by the European Commission under project number 101058518 within the HORIZON-INFRA-2021-SERV-01 call.

Data availability

This dataset, in both full-resolution HDF5 files and decimated miniSEED files, is available through International Federation of Digital Seismograph Networks (FDSN) at https://dx.doi.org/10.14470/8K802502. HDF5 files are sampled at 500 Hz, with a gauge length of 1.2 m and spacing of 5.1 m. MiniSEED files are low-pass filtered and downsampled to 125 Hz. They are further spatially decimated to one channel per 102 m.

Competing interests

The authors have no competing interests, nor do they work for, advise, own shares in, or receive funds from any organisation that could benefit from this article. They have declared no affiliations other than their research organi-

sations.

References

Allen, R. V. Automatic earthquake recognition and timing from single traces. *Bulletin of the seismological society of America*, 68(5):1521–1532, 1978. doi: 10.1785/BSSA0680051521.

Becerril, C., Sladen, A., Ampuero, J.-P., Vidal-Moreno, P. J., Gonzalez-Herraez, M., Kutschera, F., Gabriel, A.-A., and Bouchette, F. Towards tsunami early-warning with Distributed Acoustic Sensing: Expected seafloor strains induced by tsunamis [preprint]. *ESS Open Archive*, Mar. 2024. doi: 10.22541/essoar.171052484.46251426/v1.

Beyreuther, M., Barsch, R., Krischer, L., Megies, T., Behr, Y., and Wassermann, J. ObsPy: A Python Toolbox for Seismology. *Seismological Research Letters*, 81(3):530–533, 2010. doi: 10.1785/gssrl.81.3.530.

Caldeira, R. M., Marchesiello, P., Nezlin, N. P., DiGiacomo, P. M., and McWilliams, J. C. Island wakes in the southern California Bight. *Journal of Geophysical Research: Oceans*, 110(C11):0148–0227, 2005. doi: 10.1029/2004JC002675.

Corela, C. *Ocean bottom seismic noise: applications for the crust knowledge, interaction ocean-atmosphere and instrumental behaviour*. PhD thesis, Deepartamento de Engenharia Geográfica, Geofísica e Energia, Faculdade de Ciências, Universidade de Lisboa, 2014.

Crawford, W. C., Webb, S. C., and Hildebrand, J. A. Seafloor compliance observed by long-period pressure and displacement measurements. *Journal of Geophysical Research: Solid Earth*, 96(B10):16151–16160, Sept. 1991. doi: 10.1029/91jb01577.

Elgar, S., Herbers, T., and Guza, R. Reflection of ocean surface gravity waves from a natural beach. *Journal of Physical Oceanography*, 24(7):1503–1511, 1994. doi: 10.1175/1520-0485(1994)024<1503:ROOSGW>2.0.CO;2.

Flores, D. M., Sladen, A., Ampuero, J.-P., Mercerat, E. D., and Rivet, D. Monitoring Deep Sea Currents With Seafloor Distributed Acoustic Sensing. *Earth and Space Science*, 10(6), 2023. doi: 10.1029/2022ea002723.

GA 101058518, 2022. doi: 10.3030/101058518.

GA 101095055, 2023. doi: 10.3030/101095055.

GEBCO Compilation Group. GEBCO 2023 Grid, 2023. doi: 10.5285/F98B053B-0CBC-6C23-E053-6C86ABC0AF7B.

Glover, H., Wengrove, M., and Holman, R. Measuring hydrodynamics and exploring nearshore processes using distributed sensing of fiber-optic cable strain. *Coastal Engineering*, 190:104487, June 2024. doi: 10.1016/j.coastaleng.2024.104487.

Guo, Y., Marin, J. M., Ashry, I., Trichili, A., Havlik, M.-N., Ng, T. K., Duarte, C. M., and Ooi, B. S. Submarine optical fiber communication provides an unrealized deep-sea observation network. *Scientific Reports*, 13(1):15412, 2023. doi: 10.1038/s41598-023-42748-0.

Hamza, A., Sokkar, T., EL-Farahaty, K., and EL-Dessouky, H. Influence of temperature on the optical and structural properties along the diameter of optical fibres. *Optics and Lasers in Engineering*, 41(2):261–275, Feb. 2004. doi: 10.1016/s0143-8166(02)00199-9.

Herbers, T., Elgar, S., and Guza, R. Directional spreading of waves in the nearshore. *Journal of Geophysical Research: Oceans*, 104(C4):7683–7693, 1999. doi: 10.1029/1998JC900092.

Hocker, G. B. Fiber-optic sensing of pressure and temperature. *Applied Optics*, 18(9):1445, May 1979. doi: 10.1364/ao.18.001445.

Howe, B. M., Miksis-Olds, J., Rehm, E., Sagen, H., Worcester, P. F., and Haralabus, G. Observing the Oceans Acoustically. *Frontiers in Marine Science*, 6, jul 2019. doi: 10.3389/fmars.2019.00426.

Landrø, M., Bouffaut, L., Kriesell, H. J., Potter, J. R., Rørstadbotnen, R. A., Taweesintananon, K., Johansen, S. E., Brenne, J. K., Haukanes, A., Schjelderup, O., et al. Sensing whales, storms, ships and earthquakes using an Arctic fibre optic cable. *Scientific Reports*, 12(1):19226, 2022. doi: 10.1002/essoar.10507855.1.

Lindsey, N. J., Dawe, T. C., and Ajo-Franklin, J. B. Illuminating seafloor faults and ocean dynamics with dark fiber distributed acoustic sensing. *Science*, 366(6469):1103–1107, 2019. doi: 10.1126/science.aay5881.

Lindsey, N. J., Rademacher, H., and Ajo-Franklin, J. B. On the Broadband Instrument Response of Fiber-Optic DAS Arrays. *Journal of Geophysical Research: Solid Earth*, 125(2), Feb. 2020. doi: 10.1029/2019jb018145.

Loureiro, A., Schlaphorst, D., Matias, L., Pereira, A., Corela, C., Gonçalves, S., and Caldeira, R. First DAS observations from the GeoLab fibre in Madeira, Portugal. *Seismica*, 4(2), Dec. 2025. doi: 10.26443/seismica.v4i2.1482.

Marra, G., Clivati, C., Luckett, R., Tampellini, A., Kronjäger, J., Wright, L., Mura, A., Levi, F., Robinson, S., Xuereb, A., Baptie, B., and Calonico, D. Ultrastable laser interferometry for earthquake detection with terrestrial and submarine cables. *Science*, 361(6401):486–490, Aug. 2018. doi: 10.1126/science.aat4458.

Marra, G., Fairweather, D., Kamalov, V., Gaynor, P., Cantono, M., Mulholland, S., Baptie, B., Castellanos, J., Vagenas, G., Gaudron, J.-O., et al. Optical interferometry–based array of seafloor environmental sensors using a transoceanic submarine cable. *Science*, 376(6595): 874–879, 2022. doi: 10.1126/science.abo1939.

MODAS project 2022.02359.PTDC. Monitoring the Oceans with Distributed Acoustic Sensing, 2022. doi: 10.54499/2022.02359.PTDC.

Peláez Quiñones, J. D., Sladen, A., Ponte, A., Lior, I., Ampuero, J.-P., Rivet, D., Meulé, S., Bouchette, F., Pairaud, I., and Coyle, P. High resolution seafloor thermometry for internal wave and upwelling monitoring using Distributed Acoustic Sensing. *Scientific Reports*, 13 (1), Oct. 2023. doi: 10.1038/s41598-023-44635-0.

Rørstadbotnen, R. A. and Landrø, M. On the variation of ocean surface gravity wave characteristics with wind speed and direction: A case study from offshore Svalbard, Norway. *Geophysical Journal International*, page ggaf240, 2025. doi: 10.1093/gji/ggaf240.

Seabrook, B. C., Ellmauthaler, A., LeBlanc, M., Jaaskelainen, M., Maida, J. L., and Wilson, G. A. Comparison of Raman, Brillouin, and Rayleigh Distributed Temperature Measurements in High-Rate Wells. *Petrophysics – The SPWLA Journal of Formation Evaluation and Reservoir Description*, 63(6):685–699, Dec. 2022. doi: 10.30632/pjv63n6-2022a8.

Sladen, A., Rivet, D., Ampuero, J. P., De Barros, L., Hello, Y., Calbris, G., and Lamare, P. Distributed sensing of earthquakes and ocean-solid Earth interactions on seafloor telecom cables. *Nature Communications*, 10(1), Dec. 2019. doi: 10.1038/s41467-019-13793-z.

Song, Z., Zeng, X., Ni, S., Chi, B., Xu, T., Wei, Z., Jiang, W., Chen, S., and Xie, J. Near real-time in situ monitoring of nearshore ocean currents using distributed acoustic sensing on submarine fiber-optic cable. *Earth and Space Science*, 11(9):e2024EA003572, 2024. doi: 10.1029/2024EA003572.

Szczyrba, L., Mulligan, R. P., Humberston, J., Bak, A. S., McNinch, J., and Pufahl, P. K. Nearshore wave angles and directional variability during storm events. *Coastal Engineering*, 185:104372, 2023. doi: 10.5683/SP3/YI8QKQ.

Toledano, C., Ghantous, M., Lorente, P., Dalphinet, A., Aouf, L., and Sotillo, M. G. Impacts of an Altimetric Wave Data Assimilation Scheme and Currents-Wave Coupling in an Operational Wave System: The New Copernicus Marine IBI Wave Forecast Service. *Journal of Marine Science and Engineering*, 10(4):457, 2022. doi: 10.3390/jmse10040457.

UID/PRR/50019/2025, 2025. doi: 10.54499/UID/PRR/50019/2025.

Wessel, P., Luis, J. F., Uieda, L., Scharroo, R., Wobbe, F., Smith, W. H. F., and Tian, D. The Generic Mapping Tools Version 6. *Geochemistry, Geophysics, Geosystems*, 20(11):5556–5564, 2019. doi: 10.1029/2019gc008515.

Williams, E. F., Fernández-Ruiz, M. R., Magalhaes, R., Vanthillo, R., Zhan, Z., González-Herráez, M., and Martins, H. F. Distributed sensing of microseisms and teleseisms with submarine dark fibers. *Nature Communications*, 10(1), Dec. 2019. doi: 10.1038/s41467-019-13262-7.

Williams, E. F., Zhan, Z., Martins, H. F., Fernández-Ruiz, M. R., Martín-López, S., González-Herráez, M., and Callies, J. Surface Gravity Wave Interferometry and Ocean Current Monitoring With Ocean-Bottom DAS. *Journal of Geophysical Research: Oceans*, 127(5), 2022.

doi: 10.1029/2021jc018375.

Zhan, Z., Cantono, M., Kamalov, V., Mecozzi, A., Müller, R., Yin, S., and Castellanos, J. C. Optical polarization–based seismic and water wave sensing on transoceanic cables. *Science*, 371(6532):931–936, 2021. doi: 10.1126/science.abe6648.

6 Supplemental material

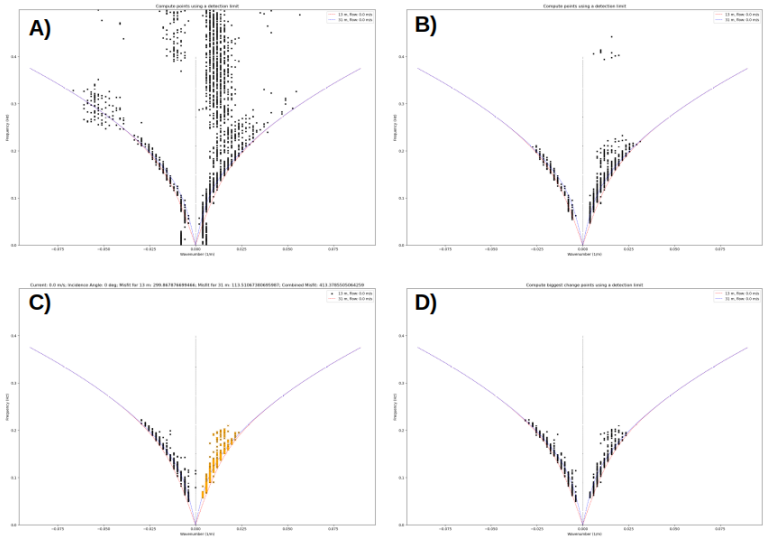

Figure S1 Examples of different detection algorithms for a DAS recording of channels 550 to 650 over a 30-minute interval, start time: 2023-10-31 03:02:29Z, downsampled to 1 Hz. (A) Detection using an STA/LTA picker with 10 wave number sample points for the short-term and 30 for the long-term average. Detected points are shown with black squares. Two basic TDCs for different depths are shown with red and blue dashed lines. The depths represent the minimum and maximum values along that section of the cable based on bathymetry information. The $k = 0$ axis is indicated by a black dotted line. (B) Same as A, but with a mask excluding points for frequencies with an amplitude smaller than 1/10 the total maximum on the respective side (land-/seaward). C) Detection of maximum amplitude on either side, including the same mask. (D) Detection of the biggest amplitude change on the outside of the maximum amplitude, including the same mask.